Journal of Materials Chemistry A

ROYAL SOCIETY OF CHEMISTRY

PAPER

View Article Online
View Journal | View Issue

Open Access Article. Published on 12 July 2023. Downloaded on 12/4/2025 10:16:46 PM. This article is licensed under a Creative Commons Attribution 3.0 Unported Licence.

Check for updates

Cite this: J. Mater. Chem. A, 2023, 11, 16104

Accelerating anhydrous proton conduction *via* anion rotation and hydrogen bond recombination: a machine-learning molecular dynamics†

Saori Minami * and Ryosuke Jinnouchi

Received 29th May 2023
Accepted 4th July 2023

DOI: 10.1039/d3ta03164k

rsc.li/materials-a

Phosphonic-acid-based electrolytes are key materials for anhydrous proton transport in fuel cells that are operatable at medium temperatures. However, these materials suffer from a severe tradeoff between proton conductivity and stability. Immobilizing phosphonic anion groups prevents anion leaching while suppressing proton transport. To reveal the origin of this relationship, we performed nanosecond-scale molecular dynamics simulations of phosphoric and phosphonic acids with different alkyl chains using machine-learned force fields. Simulations indicate that proton diffusivity is strongly correlated to the reorientation speed of anions. Thus, as the alkyl chain length increases, both the proton diffusivity and reorientation frequency decrease. Detailed analyses show that in all the materials, protons are shuttled between a pair of anions with a high frequency of approximately 10 ps^{-1}. However, only 0.1% of the shuttling protons are transported to the adjacent anion because of three orders of magnitude slower reorientation of anions that require recombination of H-bond network. Retaining the rotational freedom of anions is essential for enhancing anhydrous proton conductivity.

Introduction

Proton exchange membrane fuel cells (PEMFCs) show great potential as power sources for light- and heavy-duty vehicles.[1,2] PEMFCs employ perfluorinated ionomers as proton exchange membranes. These membranes absorb water and form heterogeneous nanosized cluster domains comprising ions and water molecules.[3–6] Under sufficiently humidified conditions, the cluster domains connect with each other and provide proton transport pathways. Owing to their high proton conductivity and chemical and mechanical stability, these membranes stably realize low ohmic resistance below the boiling temperature of water, enabling the quick starts and stops of fuel cells required for automobile applications.[6,7] However, at higher temperatures, the membranes dry up, and the proton conductivity significantly decreases. Therefore, the operational temperature and humidity are limited, and humidified inlet streams and large radiators are required to dissipate the waste heat. In addition, low-temperature operation requires purified hydrogen gas without contaminant species, such as CO, which poison the electrocatalysts. For simpler and more compact systems, advanced electrolyte materials that can extend the upper temperature limit, such as to 120 or 150 °C, are desired.[8–11]

Amphoteric molecules, such as phosphoric acid (PA) and imidazole, which act as both proton doners and accepters, are attracting attention as electrolytes that can exhibit anhydrous proton conduction at high temperatures.[12–16] PA is known to be a highly anhydrous proton-conductive electrolyte in the temperature range of 60–200 °C[15–17] and is used as an electrolyte of PA fuel cells (PAFCs). However, PAFCs have severe durability problems because PA leaches out during operation. In addition, the energy conversion efficiency of PAFCs is reduced by the low oxygen permeability and catalyst poisoning by PA anions. To improve the durability, mechanical strength, and conductivity of PAFCs, intensive studies have been conducted on the hybridization of PA with polymers, ionic liquids, and inorganic compounds.[18–26] PA-doped poly-benzimidazole (PA-PBI) exhibits a high proton conductivity in the temperature range of 100–200 °C and has been widely investigated.[14,18,23,27–29] However, this acid-doped polymer suffers from PA loss because PA does not have strong attractive interactions with polymers.[27] To enhance these interactions, Lee *et al.*[19] suggested that PA be hybridized with a relatively strong base, such as quaternary ammonium-biphosphate ion-pair-coordinated polyphenylene, which improved the PA retention from 67% in PBI to 77% after 50 h of operation at 200 °C and a relative humidity of 0%. However, higher retention is desired for practical applications. It should also be noted that PA poisoning of the catalysts is inevitable in this advanced hybrid material. To further improve the stability and performance, polymers that fix anion groups *via* covalent bonds have been proposed.[9,15,30,31] Their introduction improves the durability compared to liquid PA. However, the proton

Toyota Central R&D Labs., Inc., 41-1 Yokomichi, Nagakute, Aichi, 480-1192, Japan. E-mail: e1778@mosk.tytlabs.co.jp

† Electronic supplementary information (ESI) available. See DOI: https://doi.org/10.1039/d3ta03164k

 This journal is © The Royal Society of Chemistry 2023

Open Access Article. Published on 12 July 2023. Downloaded on 12/4/2025 10:16:46 PM. This article is licensed under a Creative Commons Attribution 3.0 Unported Licence.

conductivity is significantly decreased in these materials. Notably, the proton conductivity rapidly decreased from 350 to 43 mS cm^{-1} by connecting only one methyl group to the anion ($CH_3PO_3H_2$).[15,32] In addition, proton transport is severely hindered by the immobilization of anions. To overcome the tradeoff between proton conductivity and anion retention, the proton transport mechanism needs to be clarified.

Generally, proton transfer occurs *via* vehicle and Grotthuss mechanisms. In the vehicle mechanism, protons are transported by mobile ionic molecules. In contrast, proton transport occurs *via* sequential hopping between anions in the Grotthuss mechanism.[17,33] Ideally, the latter mechanism could significantly contribute to high proton conduction because sequential proton hopping *via* extended Grotthuss chains enables long-range proton transport without significant anion diffusion. The significant contribution of the Grotthuss mechanism to liquid PA is supported by the diffusion coefficients measured by Aihara *et al.*,[16] who showed that the diffusion coefficient of hydrogen atoms is 4.5 times larger than that of phosphorus atoms. However, in reality, sequential proton hopping requires the rearrangement of molecular anions, and thus, proton hopping and the molecular rearrangement complex interplay in proton conduction.

First principles molecular dynamics (FPMD) simulations have provided valuable insights into microscopic transport mechanisms.[34–37] An FPMD simulation by Vilčiauskas *et al.*[35] showed that long Grotthuss chains developed in neat liquid PA enables fast proton conduction. Another FPMD simulation of a mixed PA and imidazole system performed by the same group[38] showed that the Grotthuss chains were significantly shortened in the mixed system. However, applications of FPMD simulations remain scarce and have never been performed on phosphonic acid groups with alkyl chains because of their high computational cost. Accurate predictions of diffusion coefficients require sufficient statistics over hundreds pico second trajectories started from statistically uncorrelated multiple initial configurations.[39] Performing the calculations in a brute force manner is simply out of question, since the simulations on several materials require several years. Although classical MD simulations employing empirical force fields are several orders of magnitude faster than FPMD simulations, they do not accurately represent the Grotthuss mechanism, which involves bond breaking and formation in complex molecular systems. Machine-learned force fields (MLFFs)[40–48] are ideal for addressing this problem. Their flexible functional forms enable accurate reproductions of the complex FP energy landscape of the bond breaking and formation without solving the wave equation. In particular, emerging active-learning schemes coupled with reduced descriptor space[39,49] enable the efficient training of MLFFs for complex multi-elemental amorphous materials with minimum human intervention. Overall, the state-of-the-art MLFF algorithm realizes three orders of magnitude faster computations of proton transfers.

In this study, we employed the MLFF scheme to reveal the relationship between proton and anion mobilities in liquid PA (H_3PO_4) and phosphonic acids with linear alkyl chains [($C_nH_{2n+1}PO_3H_2$, n = 1, 4, and 7)]. Systematic comparisons of the four systems demonstrated that proton mobility decreases with increasing alkyl chain length, as in previously reported experiments,[15,32] and revealed a significant contribution of anion reorientation to proton transport.

Methods

Models and simulations

Liquid PA and phosphonic acids with different alkyl chain lengths were modeled using unit cells with three-dimensional periodic boundary conditions. The numbers of molecules in the unit cell are listed in Table S1,† and the models are shown in Fig. 1. In this study, we denote PA as $n_C = 0$ and $C_nH_{2n+1}PO_3H_2$ as n_C = 1, 4, and 7, where n_C denotes the number of carbon atoms in the alkyl chains.

All MD simulations for production runs were performed using the MLFF method implemented in the Vienna *Ab initio* Simulation Package (VASP).[45,50,51] MLFFs were generated using the method described later in the text. The equilibrium lattice structures of each system were determined by 100 ps-Np_zT-ensemble MD simulations at 393, 423, and 463 K and 0.1 MPa, where the symbol Np_zT refers to the cell length only along the z-direction is allowed to relax. The cell lengths in the x–y direction were fixed to prevent significant distortions in the liquid systems. The temperature and pressure were controlled by Langevin thermostat[52] and Parrinello–Rahman method,[53] respectively. For efficient equilibration, the hydrogen mass and time step (Δt) were set to 4 a.u. and 2 fs, respectively. The lattice parameters were determined as the averages over the Np_zT-ensemble MD simulations. After equilibration, 200 ps-NVT-ensemble MD simulations were conducted at 393, 423, and 463 K to examine static and dynamic properties. During the

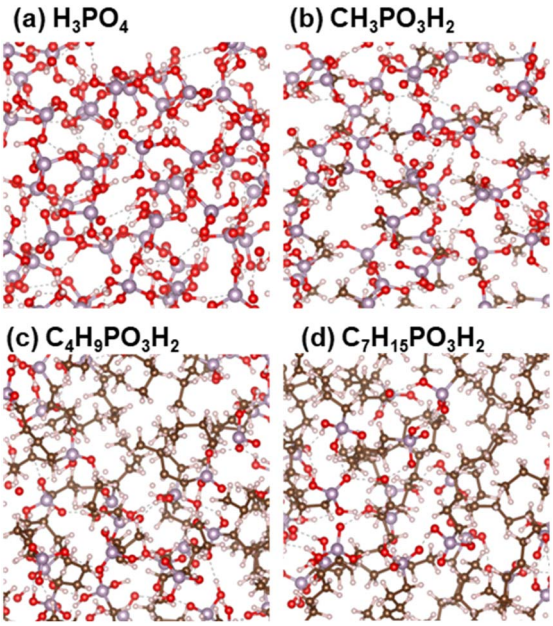

Fig. 1 Models of (a) H_3PO_4, (b) $CH_3PO_3H_2$, (c) $C_4H_9PO_3H_2$, and (d) $C_7H_{15}PO_3H_2$. White, red, brown, and purple spheres indicate H, O, C, and P atoms, respectively.

Open Access Article. Published on 12 July 2023. Downloaded on 12/4/2025 10:16:46 PM.
This article is licensed under a Creative Commons Attribution 3.0 Unported Licence.

production runs, the hydrogen mass and Δt were set to 1 a.u. and 0.5 fs, respectively.

Initial structures for the equilibrations by using MLFFs were prepared by 1 ns-NpT-ensemble classical MD simulations at 500 K and 0.1 MPa with the COMPASS[54] empirical force field and FORCITE MD package implemented in Materials Studio 2020.[55] Initial configurations for these MD simulations were prepared by the amorphous cell generator in Material Studio 2020.

Analysis of dynamical properties

The diffusion coefficients (D) of the hydrogen and phosphorus atoms were calculated from their mean square displacements (MSDs) as follows:

$$D = \frac{1}{6}\frac{\mathrm{d}}{\mathrm{d}t}\mathrm{MSD}(t) \tag{1}$$

$$\mathrm{MSD}(t) = \frac{2}{N_t N}\sum_{i=1}^{N}\sum_{j=1}^{N_t/2}\left[\mathbf{r}_i(j\Delta t + t) - \mathbf{r}_i(j\Delta t)\right]^2, \quad 0 \le t \le N_t/2\Delta t \tag{2}$$

where $N_t\Delta t$ is the total MD simulation time (200 ps). The diffusion coefficients were calculated from the slopes of the MSDs in the range of 20–100 ps. To clarify the proton transport mechanism, we examined three dynamic properties by analyzing the MD trajectories.

A previous FPMD study showed that the high proton conductivity of liquid PA owes to Grotthuss mechanism.[35] In this simulation, frequent proton hopping *via* extended Grotthuss chains was reported. The same result was also reported by a previous MD simulation using an MLFF.[49] Following the previous studies, we examined the effects of the alkyl chain length on the proton hopping frequency. The proton hopping frequency was determined as the lifetime of the electrically neutral state (H_3PO_4 for liquid PA and $C_nH_{2n+1}PO_3H_2$ for liquid phosphonic acids), which appeared and disappeared because of proton hopping between adjacent anions. The lifetime was evaluated using a method proposed in previous studies.[36,49] In this method, the number of H–O bonds per phosphorus atom at each time step is listed. From this list, a histogram $N(l\Delta t)$, which is defined as the number of neutral species that break after precisely l time steps, can be constructed. The fraction of neutral species that remains unbroken after time step m ($m = 1, \ldots, N_t$) is obtained as follows:

$$H(m\Delta t) = \frac{\sum_{l=m+1}^{N_t} N(l\Delta t)}{\sum_{l=1}^{N_t} N(l\Delta t)} \tag{3}$$

The fraction of neutral species that change from a neutral state to charged ions during time steps m and $m + 1$ is $H(m\Delta t) - H((m + 1)\Delta t)$. Lifetimes were calculated as $[m + (m + 1)]\Delta t/2$. Therefore, the average lifetime (τ_L) of molecules in the electrically neutral state can be calculated as

$$\tau_L = \sum_{m=0}^{N_t-1}\frac{1}{2}[m + (m+1)]\Delta t[H(m\Delta t) - H((m+1)\Delta t)] \tag{4}$$

The lifetime provides a timescale for proton hopping. However, as shown later, most protons shuttle only along a single H-bond between a local pair of anions within hundreds of femtoseconds and are irrelevant to progressive proton transport. A limited number of protons were progressively transferred from one anion to another and contributed to proton conduction. To reveal the timescale of these progressive proton transfers, the dynamic transitions of phosphorus atoms holding a specific proton were tracked. For this purpose, we assigned numbers to phosphorus atoms in the system and introduced a function $P_i(t)$ that records the number of phosphorus atoms in an anion holding a covalent bond with the ith proton at time t. Because the proton transfers from one anion to another *via* the Grotthuss mechanism, the number changes with time. Hence, $P_i(t)$ varies with time t. This number was defined as shown in Fig. 2. First, we assigned the number 0 to the phosphorus atom that holds the ith proton at $t = 0$. Therefore, $P_i(0)$ was equal to 0. At $t = t'$, the proton was transferred to an adjacent anion *via* an H-bond. We define the number of phosphorus atom in this proton acceptor as one. Hence, $P_i(t')$ was set to 1. At $t = t''$, the proton was transferred from the anion to an adjacent anion. If this acceptor anion contained a phosphorus atom numbered 0, then $P_i(t'')$ was set to 0. Otherwise, the phosphorus atom in the acceptor anion was assigned a value of 2, and $P_i(t'')$ was set to 2. In this manner, the phosphorus atoms were numbered, and the dynamic transition of the phosphorus atom holding the ith proton was recorded as $P_i(t)$. The average of $P_i(t)$ over i, which was defined as $P(t)$, was used to indicate the averaged number of anions a proton passed through within time range t, excluding the effects of local shuttles as well as vehicle diffusion. In other words, the time that satisfies $P(t) = 1$ indicated the average time required for a proton to move from one anion to another.

In addition to the proton hopping frequencies, we investigated the time required for reorientations of anions because the reorientation time is strongly correlated to the diffusion coefficient of the hydrogen atoms in liquid PA, a solid acid, and the coordination polymer in the previous MLFF study.[49] The reorientation time was determined from the autocorrelation function ($\langle r_{rot}(t)\rangle$) defined as:[37,49]

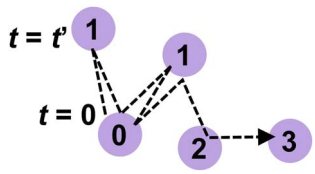

Fig. 2 Schematic of how to assign numbers of phosphorus atoms recorded in $P_i(t)$. The dashed lines indicate the trajectory of a proton transferring between anions from $t = 0$. The circles indicate the phosphorus atoms, and the numbers in the circles are recorded in $P_i(t)$.

Open Access Article. Published on 12 July 2023. Downloaded on 12/4/2025 10:16:46 PM. This article is licensed under a Creative Commons Attribution 3.0 Unported Licence.

$$\langle r_{\mathrm{rot}}(t)\rangle = \frac{2}{N_{\mathrm{t}}N_{\mathrm{PO}}}\sum_{i=1}^{N_{\mathrm{PO}}}\sum_{j=1}^{N_{\mathrm{t}}/2}\hat{\mathbf{p}}_i(j\Delta t)\cdot\hat{\mathbf{p}}_i(j\Delta t+t),\quad 0\le t\le N_{\mathrm{t}}/2\Delta t \tag{5}$$

where N_{PO} is the total number of P–O bonds. The reorientation time τ_{rot} was determined by fitting the following bi-exponential function to the autocorrelation function:[49]

$$\langle r_{\mathrm{rot}}(t)\rangle \cong c_0 \mathrm{e}^{-t/\tau_0} + (1-c_0)\mathrm{e}^{-t/\tau_{\mathrm{rot}}} \tag{6}$$

To examine the microscopic dynamical relations between reorientations and proton hopping, we further compared the function $P_i(t)$ by recording the transient of the phosphorus atom holding the ith proton, with the individual autocorrelation function defined as

$$r_{j,\mathrm{rot}}(t) = \frac{1}{N_{i,\mathrm{PO}}}\sum_{k=1}^{N_{i,\mathrm{PO}}}\hat{\mathbf{p}}_k(0)\cdot\hat{\mathbf{p}}_k(t),\quad 0\le t\le N_{\mathrm{t}} \tag{7}$$

where $\hat{\mathbf{p}}_k$ is the P–O unit vector and $N_{j,\mathrm{PO}}$ is the number of P–O bonds in the jth anion.

All analyses were performed using trajectories obtained by 200 ps MD simulations. We confirmed that D and τ_{rot} calculated from 200 ps trajectories are in good agreement with those calculated from 1 ns trajectories as shown in Fig. S1.†

Machine-learned force field

An active-learning MLFF scheme implemented in VASP[45,50,51] was used to generate the MLFFs. In this method, the potential energy of a system is written as the sum of atomic energies, similar to the Gaussian approximation potential (GAP):[41]

$$U = \sum_{i=1}^{N_{\mathrm{atom}}} U_i \tag{8}$$

where N_{atom} is the number of atoms in the unit cell. The atomic energy U_i is assumed to be a function of the descriptor $\mathbf{x}_i$ of the local environment surrounding atom i. This function is described by a linear combination of kernel functions as follows:

$$U_i = \sum_{i_{\mathrm{b}}=1}^{N_{\mathrm{b}}} w_{i_{\mathrm{b}}} K\left(\mathbf{x}_i\cdot\mathbf{x}_{i_{\mathrm{b}}}\right) \tag{9}$$

where i_{b} is the reference atom obtained from the structure in the FP training data. The expansion coefficients $\{w_{i_{\mathrm{b}}}|i_{\mathrm{b}} = 1, \ldots, N_{\mathrm{b}}\}$ were determined to optimally reproduce the FP training data. Descriptor $\mathbf{x}_i$ is a supervector constructed from the two- and three-body descriptor vectors $\mathbf{x}_i^{(2)}$ and $\mathbf{x}_i^{(3)}$, respectively:[56]

$$\mathbf{x}_i^{T} \rightarrow \left(\sqrt{\beta^{(2)}}\,\mathbf{x}_i^{(2)}, \sqrt{\beta^{(3)}}\,\mathbf{x}_i^{(3)}\right) \tag{10}$$

where the parameters $\beta^{(2)}$ and $\beta^{(3)}(=1-\beta^{(2)})$ refer to the control weights on the descriptors. The vectors $\mathbf{x}_i^{(2)}$ and $\mathbf{x}_i^{(3)}$ are composed of the expansion coefficients, ${c_n}^i$ and ${p_{n\nu l}}^i$, of the two- and three-body distribution functions, $\rho_i^{(2)}$ and $\rho_i^{(3)}$, respectively, with respect to the orthonormal radial and angular basis sets:

$$\rho_i^{(2)}(r) = \frac{1}{\sqrt{4\pi}}\sum_{\nu=1}^{N_{\mathrm{R}}} {c_n}^i \chi_{n0}(r) \tag{11}$$

$$\rho_i^{(3)}(r,s,\theta) = \sum_{l=0}^{L_{\max}}\sum_{n=1}^{N_{\mathrm{R}}}\sum_{\nu=1}^{N_{\mathrm{R}}}\sqrt{\frac{2l+1}{2}}{p_{n\nu l}}^i \chi_{nl}(r)\chi_{nl}(r)P_l(\cos\theta) \tag{12}$$

where χ_{nl} and P_l are the spherical Bessel functions and the Legendre polynomial of order l, respectively. The two-body distribution function $\rho_i^{(2)}$ is defined as follows:

$$\rho_i^{(2)}(r) = \frac{1}{4\pi}\int \rho_i(r\hat{\mathbf{r}})d\hat{\mathbf{r}} \tag{13}$$

$$\rho_i(\mathbf{r}) = \sum_{j\neq i}^{N_{\mathrm{atom}}}\tilde{\rho}_{ij}(\mathbf{r}) \tag{14}$$

$$\tilde{\rho}_{ij}(\mathbf{r}) = f_{\mathrm{cut}}(r_{ij})g(\mathbf{r}-\mathbf{r}_{ij}) \tag{15}$$

where f_{cut} is a cutoff function that smoothly removes information outside the radius R_{cut}[40] and g is the normalized Gaussian function defined as

$$g(\mathbf{r}) = \frac{1}{\sqrt{2\sigma_{\mathrm{atom}}\pi}}\exp\left(-\frac{|\mathbf{r}|^2}{2{\sigma_{\mathrm{atom}}}^2}\right) \tag{16}$$

where $\hat{\mathbf{r}}$ denotes the unit vector of $\mathbf{r}$ and $r = |\mathbf{r}|$. The three-body distribution function $\rho_i^{(3)}$ is defined as follows:

$$\rho_i^{(3)}(r,s,\theta) = \iint \delta(\hat{\mathbf{r}}\cdot\hat{\mathbf{s}} - \cos\theta)\rho_i(r\hat{\mathbf{r}})\rho_i(s\hat{\mathbf{s}})\mathrm{d}\hat{\mathbf{r}}\mathrm{d}\hat{\mathbf{s}} \tag{17}$$

The kernel function K evaluates the structural similarity between the surrounding atom i and reference atom i_{b}. The kernel function is written as a polynomial function of the inner product and is referred to as the smooth overlap of atomic positions (SOAP) which was defined by Bartók *et al.*[57] as

$$K(\mathbf{x}_i,\mathbf{x}_{i_{\mathrm{b}}}) = (\hat{\mathbf{x}}_i,\hat{\mathbf{x}}_{i_{\mathrm{b}}})^{\zeta} \tag{18}$$

where $\hat{\mathbf{x}}_i$ is a unit vector of $\mathbf{x}_i$. The normalization of $\mathbf{x}_i$ and exponentiation by ζ in eqn (18) introduces the higher-order atomic interaction terms from the two- and three-body components of $\mathbf{x}_i$.[56]

The accuracy and transferability of the MLFF are influenced by three factors: the number of structures N_{st}, number of kernels N_{b}, and descriptors $\mathbf{x}_i$ for the structures, where N_{st} provides $(3N_{\mathrm{atom}} + 7) \times N_{\mathrm{st}}$ training data, including energy, force, and stress tensor components. For the descriptor $\mathbf{x}_i$, we employ a set of parameters that enable compact representations of the local chemical environments of complex multi-elemental amorphous structures, as discussed in our previous study.[39] The parameter set is provided in Table S2.†

MLFFs are generated on the fly during MD simulations using an active-learning algorithm, which was recently improved to efficiently learn multi-elemental amorphous materials.[45] The uncertainty of the atomic energy and force for atom i predicted by the MLFF is evaluated by a spilling factor[45,58] defined as

Open Access Article. Published on 12 July 2023. Downloaded on 12/4/2025 10:16:46 PM.
This article is licensed under a Creative Commons Attribution 3.0 Unported Licence.

$$s_i = 1 - \frac{\sum_{i_b=1}^{N_b}\sum_{i'_b=1}^{N_b} K(\mathbf{x}_i, \mathbf{x}_{i_b}) K^{-1}\left(\mathbf{x}_{i_b}, \mathbf{x}_{i'_b}\right) K\left(\mathbf{x}_{i'_b}, \mathbf{x}_i\right)}{K(\mathbf{x}_i, \mathbf{x}_i)} \quad (19)$$

If either atom has an s_i value larger than 0.02, the FP calculation is conducted. The training data and reference atoms were selected using a CUR sparcification algorithm,[59] and the MLFF was updated. If all s_i values are smaller than 0.02, the atomic positions are updated by solving the equation of motion using the energy, force, and stress tensor components predicted by the MLFF. In this manner, most FP calculations are bypassed and the training data and reference atoms are efficiently selected from a wide phase space that cannot be explored using the FP method.

Unit cells smaller than those used in the production runs were used for the training runs. The numbers of molecules in the unit cell are listed in Table S3.† For all materials, isobaric MD simulations at 500 and 600 K were performed. For each temperature, a 100 ps-MD simulation was executed. The pressure was set at 0.1 MPa.

In the FP calculations for the training runs, the revised Perdew–Burke–Ernzerhof (RPBE) functional[60] with Grimme's D3 dispersion correction[61] was used to describe the exchange–correlation interactions between electrons. The Γ point was employed for the Brillouin zone integration. Plane-wave basis sets with a cutoff energy of 520 eV were used to describe the one-electron wave functions, and the projector-augmented wave (PAW) method[62,63] was used to describe the interactions between valence electrons and effective cores composed of nuclei and core electrons. The PAW atomic configurations are $1s^1$ for H, $2s^22p^2$ for C, $2s^2p^4$ for O, and $3s^23p^3$ for P.

To validate the accuracy of the MLFF produced by the parameter set in this study, preliminary 10 ps-NpT-ensemble MD simulations for the PA were performed with MLFF and FPMD. As shown in Fig. S2,† the MLFF accurately reproduced the radial distribution functions (RDFs) calculated using the FP method. The energies, forces, and stress tensor components predicted by the MLFF were also similar to those calculated using the FP method, as shown in Fig. S3.† The root mean square errors of the energy, force and stress tensor components were 2.5 meV per atom, 0.15 eV Å^{-1}, and 0.83 kbar, respectively, which were comparable to those of the conventional MLFFs.[40,41,47,48] As shown in Table S4,† the generated MLFFs realized 3000 times faster MD simulations than the FPMD method. The balanced accuracy and high efficiency allowed us to systematically compare dynamical properties relevant to the proton transfers in four materials.

Results and discussion

The proton conductivities of liquid PA and liquid phosphonic acids decreased significantly with the introduction of the alkyl chain. A previous experimental study reported that the proton conductivity decreased from 350 mS cm^{-1} for PA to 43 mS cm^{-1} by introducing only one methyl group.[15,17,32] The Nernst–Einstein equation[64,65] and proton concentrations predicted by our MD simulations (Table 1) indicate that 46% decrease (from 350 to 189 mS cm^{-1}) is attributed to the dilution of charge carriers by the introduction of methyl groups. The remaining 42% decrease to 43 mS cm^{-1} was likely attributed to the decreased diffusivity of the protons. This experimental observation was reproduced using diffusion coefficients simulated using the MLFF method. Fig. 3 shows the diffusion coefficients of hydrogen atoms (D_H) and phosphorus atoms (D_P) obtained from eqn (1) as a function of the alkyl chain length n_C. The MSDs of the hydrogen and phosphorus atoms are shown in Fig. S4.† The D_H values for $n_C = 0$ at 400 K and $n_C = 7$ at 427 K were in good agreement with the experimental values measured by pulse-gradient spin-echo (PGSE) NMR.[15,32] The diffusion coefficients of the protons (D_σ) estimated from the experimental proton conductivity at 400 K[15,32] using the Nernst–Einstein equation are also shown in Fig. 3a. The estimated D_σ is reproduced by the D_H values obtained by the MD simulations. The D_H values decreases by 60% upon introducing a methyl group to the molecule, whereas the D_P values are nearly constant independent of n_C. For all n_C values at all temperatures, the D_H values were larger than the D_P values (Fig. 3c). The D_H/D_P ratio decreased with increasing n_C values. The D_H/D_P ratio did not depend strongly on the temperature, although both the D_H and D_P values increased with increasing temperatures. D_H is larger than D_P because hydrogen diffusion involves both the Grotthuss and vehicle mechanisms,[16,35] whereas phosphorus atoms diffuse only *via* the vehicle mechanism. The decrease in D_H/D_P with increasing n_C indicated that the Grotthuss mechanism was suppressed by the alkyl chains. The small dependence of D_H/D_P on the temperature indicates that the suppression of the Grotthuss mechanism by the alkyl chains occurs at all temperature ranges.

Table 1 Densities and proton concentrations predicted by molecular dynamics simulations

Number of carbon atoms (n_C)	T (K)	Density (g cm^{-3})	Proton concentration (mmol cm^{-3})
0	393	1.74	53.3
	423	1.73	53.1
	463	1.71	52.5
1	393	1.38	28.7
	423	1.38	28.7
	463	1.36	28.3
4	393	1.09	15.8
	423	1.11	16.1
	463	1.10	16.0
7	393	0.892	11.3
	423	0.906	11.3
	463	0.900	10.8

Fig. 4 compares the RDFs and running integration numbers (RINs) for P–P and O–H pairs. The first peak of the RDF of the P–P pairs (g_{PP}) indicates that the average nearest neighbor distance of the anions is 4.7 Å. The height of the first peak increased and the RIN at the first peak decreased as n_C increased. This trend indicates that the anions are diluted and localized with increasing n_C. The first peak of g_{OH} at 1.1 Å is attributed to the intramolecular covalent O–H bonds, and the

Open Access Article. Published on 12 July 2023. Downloaded on 12/4/2025 10:16:46 PM.
This article is licensed under a Creative Commons Attribution 3.0 Unported Licence.

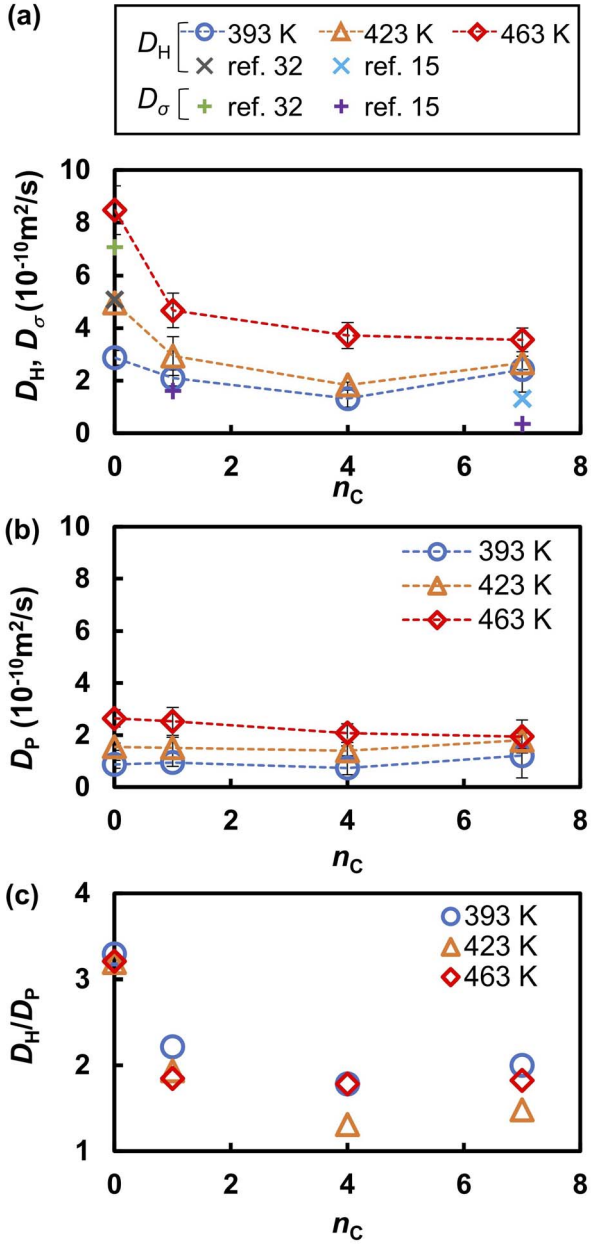

Fig. 3 (a) Diffusion coefficients hydrogen atoms and protons (D_H and D_σ, respectively), (b) the diffusion coefficient of phosphorus atoms (D_P), and (c) their ratio (D_H/D_P) as functions of the alkyl chain length (n_C). Experimental values of D_H for $n_C = 0$ at 400 K and $n_C = 7$ at 427 K are taken from ref. 15 and 32, respectively. The experimental proton conductivity used to estimate the values of D_σ *via* the Nernst–Einstein equation are taken from ref. 15 and 32.

second peak at 1.5 Å is attributed to intermolecular hydrogen bonds (O···H–O). As observed in previous FPMD and MLFF studies[36,49] of liquid PA, these peaks overlapped regardless of the alkyl chain length, indicating that protons were frequently transferred between adjacent anions. The intensity of the hydrogen bonds peak decreases with increasing n_C values, and the RINs of hydrogen bonds between phosphonic acid anions, which is evaluated from the n_{OH} at 2.2 Å, decreases from 1.9 at $n_C = 0$ to 1.3 at $n_C = 7$.

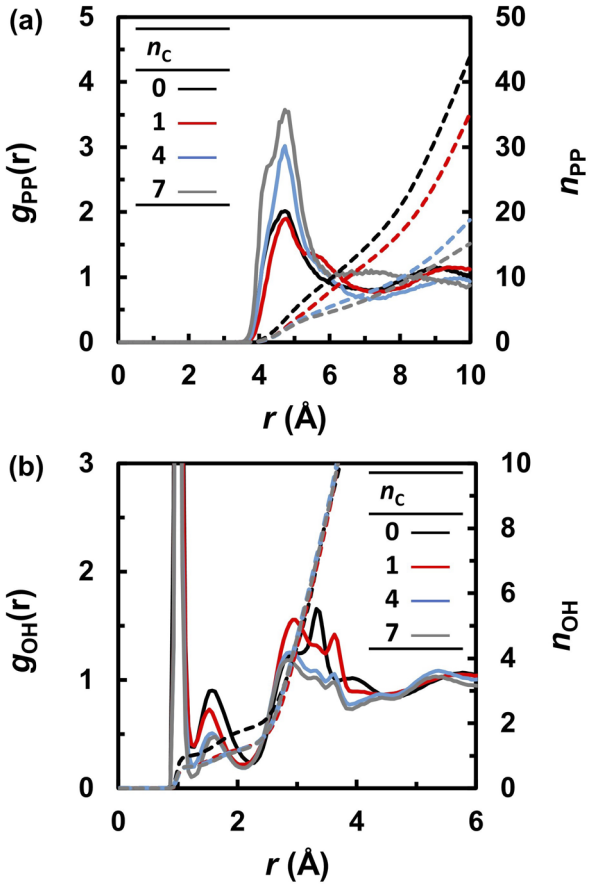

Fig. 4 Radial distribution functions (solid lines) and running integration numbers (dashed lines) of (a) P–P and (b) O–H for various n_C values at 463 K.

The frequent proton transfer between adjacent anions is supported by the lifetime τ_L of the neutral species (H_3PO_4 and $C_nH_{2n+1}PO_3H_2$), which were calculated using eqn (4). The lifetime τ_L at 463 K is shown as a function of the alkyl chain length n_C in Fig. 5a. The lifetime τ_L increased from 100 to 300 fs with an increase in n_C. These results indicate that the proton hopping frequency decreases with increasing n_C values. This trend also appeared in the probability of finding a neutral state in the MD trajectories. As shown in Fig. 5b, the probability gradually increased with increasing n_C values. Hence, it was concluded that alkyl chains hinder proton hopping. However, the proton hopping frequency was high and did not correlate with the D_H values. For example, D_H significantly decreased from $n_C = 0$ to 1, whereas τ_L did not change significantly. This indicates that proton hopping does not dominate proton transport.

Previous FPMD and MLFF studies indicated that the molecular reorientation involved in proton transport strongly influences the proton diffusivity in liquid PA, solid acids, and coordination polymers containing PA anions.[37,49] A similar trend, but a clearer correlation, was observed in the liquid PA and phosphonic acid electrolytes examined in this study. Table 2 summarizes the reorientation times τ_{rot} of the anions, as determined from the autocorrelation function in eqn (6). Under all conditions, the reorientation time τ_{rot} was three orders of

Open Access Article. Published on 12 July 2023. Downloaded on 12/4/2025 10:16:46 PM.
This article is licensed under a Creative Commons Attribution 3.0 Unported Licence.

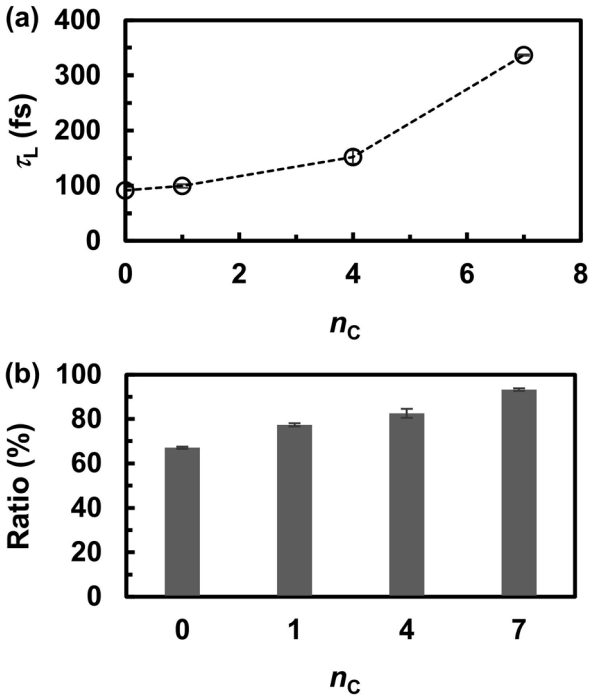

Fig. 5 (a) The lifetime (τ_L) of electrically neutral species (H_3PO_4 and $C_nH_{2n+1}PO_3H_2$) at 463 K and (b) probability of finding neutral species during the molecular dynamics simulations.

Table 2 Relaxation time (τ_{rot}) of anion reorientation

Number of carbons(n_C)	Temperature (K)	τ_{rot} (ps)
0	393	78.0
	423	44.1
	463	26.5
1	393	104
	423	64.8
	463	44.1
4	393	226
	423	170
	463	67.9
7	393	342
	423	214
	463	131

magnitude longer than that of proton hopping, as shown in Fig. 5. The value of τ_{rot} computed for liquid PA is close to the reorientation correlation time of the 10 ps timescale for ^1H–^1H dipolar interactions in liquid PA measured by PGSE NMR.[16] At 463 K, the reorientation time increased from 26 to 130 ps as the alkyl chain length increased from 0 to 7. The same trend was observed at 393 and 423 K. It should also be noted that the frequency of reorientation, defined as the inverse of τ_{rot}, is strongly correlated with D_H, as shown in Fig. 6. This indicates that anion reorientation limits proton transport. The reorientation was decelerated by increasing the alkyl chain length, which likely led to slower hydrogen diffusion.

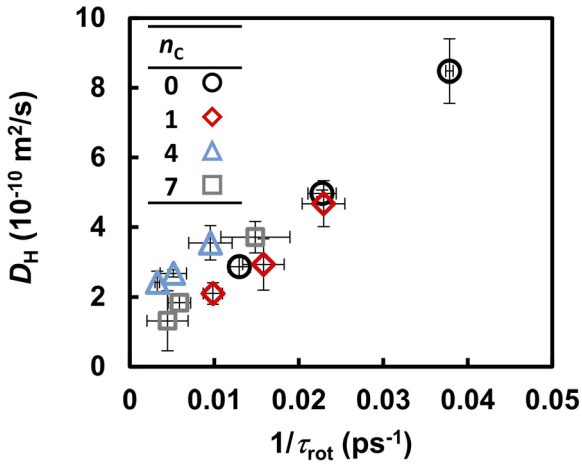

Fig. 6 Correlation between the anion reorientation frequency ($1/\tau_{rot}$) and diffusion coefficient of hydrogen atoms (D_H).

Fig. 3 suggests that the Grotthuss mechanism is suppressed by the alkyl chains. However, the proton hopping frequency shown in Fig. 5 was high and could not be strongly correlated with the D_H. In contrast, the reorientation frequency exhibited a strong correlation with D_H although its timescale was three times longer than that of proton hopping. To reveal the mechanism by which anion reorientation participates in proton transport, we examined the number of phosphorus atoms $P(t)$ that a proton crossed up to time t. The computed $P(t)$ values at 463 K are shown in Fig. 7. The value of $P(t)$ decreased with increasing n_C values. Notably, in all the electrolytes, $P(t)$ reaches 0.7 ± 0.1 at $t = \tau_{rot}$, as indicated by the yellow band in Fig. 7. This result means that roughly 70% of protons transported from one anion to the other every anion rotation by 90°.

To further reveal the microscopic dynamic mechanisms, we compared the number $P_i(t)$ of the ith proton with the autocorrelation $r_{j,rot}(t)$ of a phosphonic anion that passes the ith proton from one adjacent anion to the other as shown in Fig. 8. Four snapshots of the proton transfer at $t = t_1$, t_2, t_3, and t_4 are shown

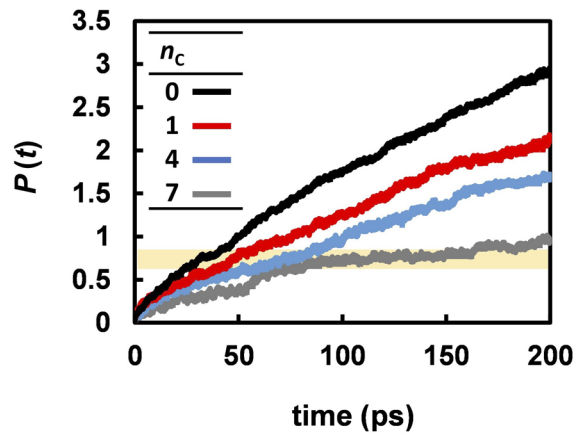

Fig. 7 The average number of anions that a proton passes through within the time range t.

Open Access Article. Published on 12 July 2023. Downloaded on 12/4/2025 10:16:46 PM.
This article is licensed under a Creative Commons Attribution 3.0 Unported Licence.

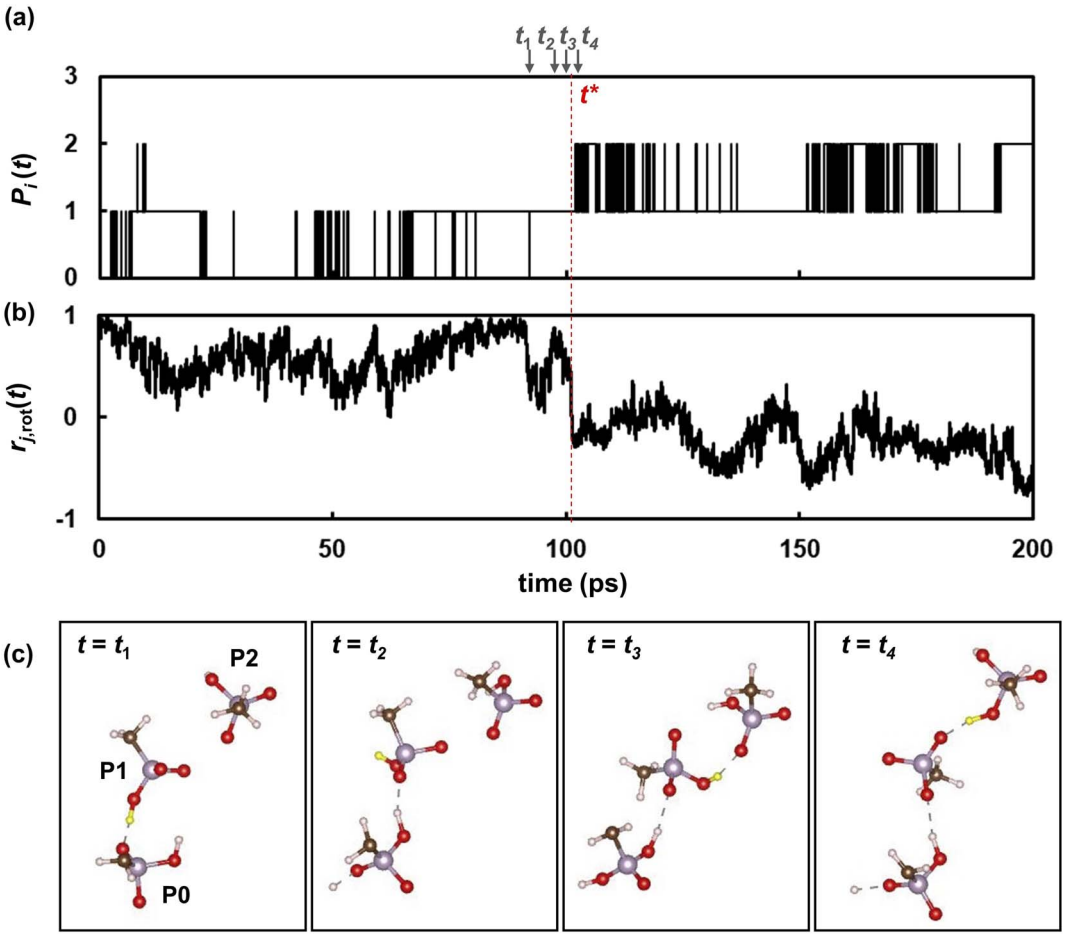

Fig. 8 (a) The number of phosphorus atom [$P_i(t)$] in an anion holding a covalent bond with the ith proton shown as the yellow sphere. (b) The autocorrelation function $r_{j,\mathrm{rot}}(t)$ of the anion P1 passing the ith proton from the anion P0 to the anion P2. (c) Snapshots of three anions (P0, P1 and P2) at $t = t_1$, t_2, t_3, and t_4 near the transition time of $t = t^*$.

in the same figure. In these snapshots, the ith proton is indicated by a yellow sphere. As shown in Fig. 8a, $P_i(t)$ initially oscillates between 0 and 1, indicating that the proton shuttles between the phosphonic anions P0 and P1 in Fig. 8c. At $t = t_2$, the pair of anions formed an H-bond *via* another proton, as shown in the second snapshot in Fig. 8c. This induces a remarkably fast rotation of anion P1 at $t = t_3$, which leads to a significant decrease in the autocorrelation functions $r_{j,\mathrm{rot}}(t)$ of anion P1, as shown in Fig. 8b. This rotation allows anion P1 to form a H-bond with another anion, P2, *via* the ith proton. At $t =$ 101 ps (denoted as t^*), slightly after $t = t_3$, the ith proton is transferred from P1 to another anion (P2). Therefore, $P_i(t)$ increases from 1 to 2. Atomic-scale dynamics clearly indicate that progressive proton transfer occurs when the anions rotate. Thus, anion rotation limits proton transport. However, it should be noted that rotations are strongly correlated with the recombination dynamics of H-bonds because additional H-bond formation at $t = t_2$ promotes anion rotation. Hence, concerted anion rotation and H-bond recombination enabled high proton conductivity. Based on this mechanism, we estimated the proton diffusion coefficients. As shown in Fig. 7, 70% of protons are transferred to adjacent anions every anion rotation. This means that 70% of protons move by the nearest neighbor P–P distance Δr_{PP} of 4.7 Å per reorientation time τ_{rot} on average. This mechanism leads to the diffusion coefficient of $D_{\mathrm{rot}} = 0.70 \times \langle \Delta r_{\mathrm{PP}}{}^2 \rangle / 6\tau_{\mathrm{rot}}$. As shown in Fig. 9 and 3a, D_{rot} agrees reasonably well with the D_{H} calculated using the MSDs.

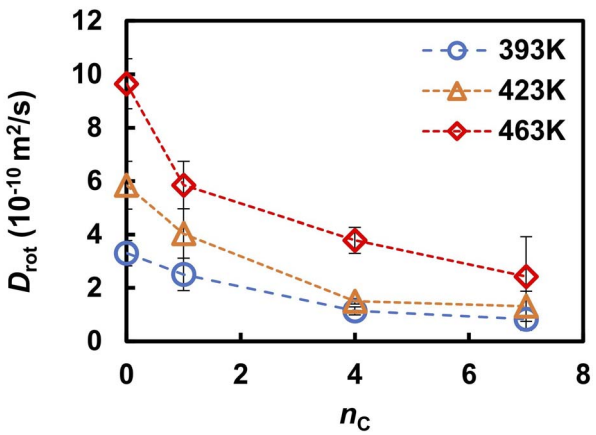

Fig. 9 D_{rot} as a function of the n_{C}.

Open Access Article. Published on 12 July 2023. Downloaded on 12/4/2025 10:16:46 PM.
This article is licensed under a Creative Commons Attribution 3.0 Unported Licence.

Conclusions

The origin of the decrease in proton diffusivity with an increasing number of alkyl chains to phosphonic acid groups was investigated by MD simulations employing MLFFs. Our systematic MD simulations of liquid PA and phosphonic acids indicated that in all materials, the protons were shuttle between a pair of anions with a high frequency of approximately 10 ps^{-1}. However, only 0.1% of the shuttling protons were successfully transported to adjacent anions. This was due to the speed of the anion reorientation, which is three orders of magnitude slower than that of the proton hopping. Detailed atomic-scale dynamic analyses revealed that an anion could only pass a proton from one adjacent anion to another when rotating. This rotation was promoted by the recombination of H-bonds. Hence, concerted rotation and H-bond recombination are indispensable for proton conduction. When phosphonic acid anions are bonded to alkyl chains, increasing the alkyl chain length caused a significant deceleration of the anion rotation, which led to the suppression of fast Grotthuss proton transfer. Accordingly, retaining the rotational freedom of anions as well as H-bond recombination is the key to balancing the proton conductivity and stability of anhydrous proton-conductive electrolytes based on phosphoric and phosphonic acid anions. Based on the present results and past studies, we can consider several approaches, such as acid/base ion pairs,[19] solid acids,[49] and their hybridizations, which retain high rotational motions of anions and prevent reaching out of anions. As demonstrated by Lee and co-workers,[19] acid/base ion pairs achieved high anion retention in durability tests while retained the high proton conductivity due to the attractive interaction between the ions. Although further high durability is required for practical applications, we expect that proper designs of acid and base molecules can realize balanced conductivity and durability. Solid acids in the high-temperature phase achieved the high proton conductivity owing to high anion rotations in their cation frame as shown in our previous MLFF study.[49] Although their poor water resistances are the problem, we expect that a variety of frame architectures, such as metal- and covalent-organic frameworks,[66,67] will provide flexible designing of proton conducting mediums. We believe that high anion rotation is a key to designing proton conductive materials, and the MLFF will provide a useful platform to explore the new materials *in silico*.

Conflicts of interest

The authors declare that they have no competing financial interests or personal relationships that may have influenced the research reported in this study.

Acknowledgements

This study was partially supported by NEDO (New Energy and Industrial Technology Development Organization) financially. The authors wish to acknowledge Professor Osamu Yamamuro for fruitful discussion.

Notes and references

1 D. A. Cullen, K. Neyerlin, R. K. Ahluwalia, R. Mukundan, K. L. More, R. L. Borup, A. Z. Weber, D. J. Myers and A. Kusoglu, New roads and challenges for fuel cells in heavy-duty transportation, *Nat. Energy*, 2021, **6**(5), 462–474.
2 T. Yoshida and K. Kojima, Toyota MIRAI fuel cell vehicle and progress toward a future hydrogen society, *Electrochem. Soc. Interface*, 2015, **24**(2), 45–49.
3 M. Falk, An infrared study of water in perfluorosulfonate (Nafion) membranes, *Can. J. Chem.*, 1980, **58**(14), 1495–1501.
4 T. D. Gierke, G. Munn and F. Wilson, The morphology in nafion perfluorinated membrane products, as determined by wide-and small-angle x-ray studies, *J. Polym. Sci., Polym. Phys. Ed.*, 1981, **19**(11), 1687–1704.
5 J.-C. Perrin, S. Lyonnard and F. Volino, Quasielastic neutron scattering study of water dynamics in hydrated nafion membranes, *J. Phys. Chem. C*, 2007, **111**(8), 3393–3404.
6 A. Kusoglu and A. Z. Weber, New insights into perfluorinated sulfonic-acid ionomers, *Chem. Rev.*, 2017, **117**(3), 987–1104.
7 S. Samms, S. Wasmus and R. Savinell, Thermal stability of Nafion® in simulated fuel cell environments, *J. Electrochem. Soc.*, 1996, **143**(5), 1498–1504.
8 E. Qu, X. Hao, M. Xiao, D. Han, S. Huang, Z. Huang, S. Wang and Y. Meng, Proton exchange membranes for high temperature proton exchange membrane fuel cells: challenges and perspectives, *J. Power Sources*, 2022, **533**, 231386.
9 K. H. Lim, A. S. Lee, V. Atanasov, J. Kerres, E. J. Park, S. Adhikari, S. Maurya, L. D. Manriquez, J. Jung and C. Fujimoto, Protonated phosphonic acid electrodes for high power heavy-duty vehicle fuel cells, *Nat. Energy*, 2022, **7**(3), 248–259.
10 New Energy and Industrial Technology Development Organization (NEDO), *Fuel Cell Development Progress 2022 Report*. **https://www.nedo.go.jp/content/100944011.pdf**.
11 R. Haider, Y. Wen, Z.-F. Ma, D. P. Wilkinson, L. Zhang, X. Yuan, S. Song and J. Zhang, Proton exchange membranes for high temperature proton exchange membrane fuel cells: challenges and perspectives, *Chem. Soc. Rev.*, 2021, **50**(2), 1138–1187.
12 A. S. Lee, Y.-K. Choe, I. Matanovic and Y. S. Kim, The energetics of phosphoric acid interactions reveals a new acid loss mechanism, *J. Mater. Chem. A*, 2019, **7**(16), 9867–9876.
13 E. Quartarone, S. Angioni and P. Mustarelli, Polymer and Composite Membranes for Proton-Conducting, High-Temperature Fuel Cells: A Critical Review, *Materials*, 2017, **10**(7), 687.
14 A. Schechter and R. F. Savinell, Imidazole and 1-methyl imidazole in phosphoric acid doped polybenzimidazole, electrolyte for fuel cells, *Solid State Ionics*, 2002, **147**(1–2), 181–187.
15 H. Steininger, M. Schuster, K. Kreuer, A. Kaltbeitzel, B. Bingöl, W. H. Meyer, S. Schauff, G. Brunklaus, J. Maier and H. W. Spiess, Intermediate temperature proton

Open Access Article. Published on 12 July 2023. Downloaded on 12/4/2025 10:16:46 PM. This article is licensed under a Creative Commons Attribution 3.0 Unported Licence.

conductors for PEM fuel cells based on phosphonic acid as protogenic group: a progress report, *Phys. Chem. Chem. Phys.*, 2007, **9**(15), 1764–1773.

16 Y. Aihara, A. Sonai, M. Hattori and K. Hayamizu, Ion conduction mechanisms and thermal properties of hydrated and anhydrous phosphoric acids studied with 1H, 2H, and 31P NMR, *J. Phys. Chem. B*, 2006, **110**(49), 24999–25006.

17 T. Norby, Solid-state protonic conductors: principles, properties, progress and prospects, *Solid State Ionics*, 1999, **125**(1–4), 1–11.

18 J. Wainright, J. T. Wang, D. Weng, R. Savinell and M. Litt, Acid-doped polybenzimidazoles: a new polymer electrolyte, *J. Electrochem. Soc.*, 1995, **142**(7), L121–L123.

19 K.-S. Lee, J. S. Spendelow, Y.-K. Choe, C. Fujimoto and Y. S. Kim, An operationally flexible fuel cell based on quaternary ammonium-biphosphate ion pairs, *Nat. Energy*, 2016, **1**(9), 1–7.

20 S. M. Haile, D. A. Boysen, C. R. Chisholm and R. B. Merle, Solid acids as fuel cell electrolytes, *Nature*, 2001, **410**(6831), 910–913.

21 S. M. Haile, C. R. Chisholm, K. Sasaki, D. A. Boysen and T. Uda, Solid acid proton conductors: from laboratory curiosities to fuel cell electrolytes, *Faraday Discuss.*, 2007, **134**, 17–39.

22 D. A. Boysen, T. Uda, C. R. Chisholm and S. M. Haile, High-performance solid acid fuel cells through humidity stabilization, *Science*, 2004, **303**(5654), 68–70.

23 O. Kongstein, T. Berning, B. Børresen, F. Seland and R. Tunold, Polymer electrolyte fuel cells based on phosphoric acid doped polybenzimidazole (PBI) membranes, *Energy*, 2007, **32**(4), 418–422.

24 S. Horike, D. Umeyama, M. Inukai, T. Itakura and S. Kitagawa, Coordination-network-based ionic plastic crystal for anhydrous proton conductivity, *J. Am. Chem. Soc.*, 2012, **134**(18), 7612–7615.

25 D. Umeyama, S. Horike, M. Inukai, T. Itakura and S. Kitagawa, Inherent proton conduction in a 2D coordination framework, *J. Am. Chem. Soc.*, 2012, **134**(30), 12780–12785.

26 V. Atanasov, A. S. Lee, E. J. Park, S. Maurya, E. D. Baca, C. Fujimoto, M. Hibbs, I. Matanovic, J. Kerres and Y. S. Kim, Synergistically integrated phosphonated poly (pentafluorostyrene) for fuel cells, *Nat. Mater.*, 2021, **20**(3), 370–377.

27 J. Chen, L. Wang and L. Wang, Highly conductive polybenzimidazole membranes at low phosphoric acid uptake with excellent fuel cell performances by constructing long-range continuous proton transport channels using a metal–organic framework (UIO-66), *ACS Appl. Mater. Interfaces*, 2020, **12**(37), 41350–41358.

28 S. Zhu, L. Yan, D. Zhang and Q. Feng, Molecular dynamics simulation of microscopic structure and hydrogen bond network of the pristine and phosphoric acid doped polybenzimidazole, *Polymer*, 2011, **52**(3), 881–892.

29 S. Pahari, C. K. Choudhury, P. R. Pandey, M. More, A. Venkatnathan and S. Roy, Molecular dynamics simulation of phosphoric acid doped monomer of polybenzimidazole: a potential component polymer electrolyte membrane of fuel cell, *J. Phys. Chem. B*, 2012, **116**(24), 7357–7366.

30 T. Rager, M. Schuster, H. Steininger and K. D. Kreuer, Poly (1, 3-phenylene-5-phosphonic Acid), a Fully Aromatic Polyelectrolyte with High Ion Exchange Capacity, *Adv. Mater.*, 2007, **19**(20), 3317–3321.

31 M. Tanaka, Y. Takeda, T. Wakiya, Y. Wakamoto, K. Harigaya, T. Ito, T. Tarao and H. Kawakami, Acid-doped polymer nanofiber framework: three-dimensional proton conductive network for high-performance fuel cells, *J. Power Sources*, 2017, **342**, 125–134.

32 J.-P. Melchior, K.-D. Kreuer and J. Maier, Proton conduction mechanisms in the phosphoric acid–water system ($H_4P_2O_7$–$H_3PO_4 \cdot 2H_2O$): a ^{1}H, ^{31}P and ^{17}O PFG-NMR and conductivity study, *Phys. Chem. Chem. Phys.*, 2017, **19**(1), 587–600.

33 K.-D. Kreuer, Proton conductivity: materials and applications, *Chem. Mater.*, 1996, **8**(3), 610–641.

34 Y.-K. Choe, E. Tsuchida, T. Ikeshoji, S. Yamakawa and S.-a. Hyodo, Nature of proton dynamics in a polymer electrolyte membrane, nafion: a first-principles molecular dynamics study, *Phys. Chem. Chem. Phys.*, 2009, **11**(20), 3892–3899.

35 L. Vilčiauskas, M. E. Tuckerman, G. Bester, S. J. Paddison and K.-D. Kreuer, The mechanism of proton conduction in phosphoric acid, *Nat. Chem.*, 2012, **4**(6), 461–466.

36 E. Tsuchida, Ab initio molecular-dynamics simulation of concentrated phosphoric acid, *J. Phys. Soc. Jpn.*, 2006, **75**(5), 054801.

37 C. Dreßler and D. Sebastiani, Effect of anion reorientation on proton mobility in the solid acids family CsH_yXO_4 (X = S, P, Se, y = 1, 2) from ab initio molecular dynamics simulations, *Phys. Chem. Chem. Phys.*, 2020, **22**(19), 10738–10752.

38 L. Vilčiauskas, M. E. Tuckerman, J. P. Melchior, G. Bester and K.-D. Kreuer, First principles molecular dynamics study of proton dynamics and transport in phosphoric acid/imidazole (2: 1) system, *Solid State Ionics*, 2013, **252**, 34–39.

39 R. Jinnouchi, S. Minami, F. Karsai, C. Verdi and G. Kresse, Proton Transport in Perfluorinated Ionomer Simulated by Machine-Learned Interatomic Potential, *J. Phys. Chem. Lett.*, 2023, **14**(14), 3581–3588.

40 J. Behler and M. Parrinello, Generalized neural-network representation of high-dimensional potential-energy surfaces, *Phys. Rev. Lett.*, 2007, **98**(14), 146401.

41 A. P. Bartók, M. C. Payne, R. Kondor and G. Csányi, Gaussian approximation potentials: the accuracy of quantum mechanics, without the electrons, *Phys. Rev. Lett.*, 2010, **104**(13), 136403.

42 A. V. Shapeev, Moment Tensor Potentials: A Class of Systematically Improvable Interatomic Potentials, *Multiscale Model. Simul.*, 2016, **14**(3), 1153–1173.

43 L. Zhang, J. Han, H. Wang, R. Car and W. E, Deep Potential Molecular Dynamics: A Scalable Model with the Accuracy of Quantum Mechanics, *Phys. Rev. Lett.*, 2018, **120**(14), 143001.

Open Access Article. Published on 12 July 2023. Downloaded on 12/4/2025 10:16:46 PM.
This article is licensed under a Creative Commons Attribution 3.0 Unported Licence.

44 K. T. Schutt, H. E. Sauceda, P. J. Kindermans, A. Tkatchenko and K. R. Muller, SchNet - a deep learning architecture for molecules and materials, *J. Chem. Phys.*, 2018, **148**(24), 241722.
45 R. Jinnouchi, F. Karsai and G. Kresse, On-the-fly machine learning force field generation: application to melting points, *Phys. Rev. B*, 2019, **100**(1), 014105.
46 R. Drautz, Atomic cluster expansion for accurate and transferable interatomic potentials, *Phys. Rev. B*, 2019, **99**(1), 014104.
47 A. E. Allen, G. Dusson, C. Ortner and G. Csányi, Atomic permutationally invariant polynomials for fitting molecular force fields, *Mach. Learn.:Sci. Technol.*, 2021, **2**(2), 025017.
48 S. Batzner, A. Musaelian, L. Sun, M. Geiger, J. P. Mailoa, M. Kornbluth, N. Molinari, T. E. Smidt and B. Kozinsky, E (3)-equivariant graph neural networks for data-efficient and accurate interatomic potentials, *Nat. Commun.*, 2022, **13**(1), 1–11.
49 R. Jinnouchi, Molecular dynamics simulations of proton conducting media containing phosphoric acid, *Phys. Chem. Chem. Phys.*, 2022, **24**(25), 15522–15531.
50 G. Kresse and J. Furthmüller, Efficient iterative schemes for ab initio total-energy calculations using a plane-wave basis set, *Phys. Rev. B: Condens. Matter Mater. Phys.*, 1996, **54**(16), 11169.
51 G. Kresse and J. Furthmüller, Efficiency of ab-initio total energy calculations for metals and semiconductors using a plane-wave basis set, *Comput. Mater. Sci.*, 1996, **6**(1), 15–50.
52 M. P. Allen and D. J. Tildesley, *Computer Simulation of Liquids*, Oxford University Press, 2017.
53 M. Parrinello and A. Rahman, Crystal structure and pair potentials: a molecular-dynamics study, *Phys. Rev. Lett.*, 1980, **45**(14), 1196–1199.
54 H. Sun, COMPASS: an ab initio force-field optimized for condensed-phase applications overview with details on alkane and benzene compounds, *J. Phys. Chem. B*, 1998, **102**(38), 7338–7364.
55 *BIOVIA Materials Studio*, Dassault, San Diego, 2020.
56 R. Jinnouchi, F. Karsai, C. Verdi, R. Asahi and G. Kresse, Descriptors representing two-and three-body atomic distributions and their effects on the accuracy of machine-learned inter-atomic potentials, *J. Chem. Phys.*, 2020, **152**(23), 234102.
57 A. P. Bartók, R. Kondor and G. Csányi, On representing chemical environments, *Phys. Rev. B*, 2013, **87**(18), 184115.
58 K. Miwa and H. Ohno, Interatomic potential construction with self-learning and adaptive database, *Phys. Rev. Mater.*, 2017, **1**(5), 053801.
59 M. W. Mahoney and P. Drineas, CUR matrix decompositions for improved data analysis, *Proc. Natl. Acad. Sci. U. S. A.*, 2009, **106**(3), 697–702.
60 B. Hammer, L. B. Hansen and J. K. Nørskov, Improved adsorption energetics within density-functional theory using revised Perdew-Burke-Ernzerhof functionals, *Phys. Rev. B: Condens. Matter Mater. Phys.*, 1999, **59**(11), 7413–7421.
61 S. Grimme, J. Antony, S. Ehrlich and H. Krieg, A consistent and accurate ab initio parametrization of density functional dispersion correction (DFT-D) for the 94 elements H-Pu, *J. Chem. Phys.*, 2010, **132**(15), 154104.
62 P. E. Blöchl, Projector augmented-wave method, *Phys. Rev. B: Condens. Matter Mater. Phys.*, 1994, **50**(24), 17953–17979.
63 G. Kresse and D. Joubert, From ultrasoft pseudopotentials to the projector augmented-wave method, *Phys. Rev. B: Condens. Matter Mater. Phys.*, 1999, **59**(3), 1758–1775.
64 T. A. Zawodzinski Jr, M. Neeman, L. O. Sillerud and S. Gottesfeld, Determination of water diffusion coefficients in perfluorosulfonate ionomeric membranes, *J. Phys. Chem.*, 1991, **95**(15), 6040–6044.
65 S. Ochi, O. Kamishima, J. Mizusaki and J. Kawamura, Investigation of proton diffusion in Nafion® 117 membrane by electrical conductivity and NMR, *Solid State Ionics*, 2009, **180**(6–8), 580–584.
66 N. Ma and S. Horike, Metal-Organic Network-Forming Glasses, *Chem. Rev.*, 2022, **122**(3), 4163–4203.
67 H. Xu, S. Tao and D. Jiang, Proton conduction in crystalline and porous covalent organic frameworks, *Nat. Mater.*, 2016, **15**(7), 722–726.

 This journal is © The Royal Society of Chemistry 2023